aerospace

Article

Large Eddy Simulation of Pulsed Film Cooling with a Dielectric Barrier Discharge Plasma Actuator

Zhou Shen, Beimeng Hu, Guozhan Li * and Hongjun Zhang

College of Metrology and Measurement Engineering, China Jiliang University, Hangzhou 310018, China; cjlushen1201@163.com (Z.S.); bmhu8117@163.com (B.H.); zhanghongjun@cjlu.edu.cn (H.Z.)
* Correspondence: liguozhan@cjlu.edu.cn

Abstract: The effects of the coolant pulsation and the plasma aerodynamic actuation (PAA) on the film cooling are herein explored via large eddy simulations. The electrohydrodynamic force derived from the PAA was solved through the phenomenological plasma model. The Strouhal number of the sinusoidal coolant pulsation and the averaged pulsation blowing ratio were 0.25 and 1.0, respectively. Comprehensive analyses were carried out on the time-averaged flow fields, and the results reveal that the pulsed cooling jet might cause a deeper penetration into the crossflow, and this phenomenon could be remarkably mitigated by the downward force of the PAA. Comparing steady film cooling to pulsed film cooling revealed a modest 15.1% reduction in efficiency, while the application of the dielectric barrier discharge plasma actuator (DBDPA) substantially enhanced the pulsed film cooling efficiency by 42.1%. Moreover, the counter-rotating vortex pair (CRVP) was enlarged and lifted off from the wall more poorly due to the coolant pulsation, and the PAA weakened the detrimental lift-off effect and entrainment of the CRVP. Then, the spatial–temporal development of the coherent structures was figured out by the alterations in the centerline temperature, reflecting the formation of the intermittent coherent structures rather than hairpin vortices due to the coolant pulsation, and their size and upcast behaviors were reduced by the PAA; thus, the turbulent integration of the coolant with the crossflow was suppressed fundamentally. Finally, the three-dimensional streamlines confirmed that the coherent structure dynamic behaviors were significantly regulated by the PAA for alleviating the adverse influences of the coolant pulsation. In summary, the PAA can effectively improve the pulsed film cooling efficiency by controlling the spatial–temporal development of the dominant coherent structures.

Keywords: pulsed film cooling; large eddy simulation; coherent structure; film cooling efficiency

Citation: Shen, Z.; Hu, B.; Li, G.; Zhang, H. Large Eddy Simulation of Pulsed Film Cooling with a Dielectric Barrier Discharge Plasma Actuator. *Aerospace* **2024**, *11*, 28. https://doi.org/10.3390/aerospace11010028

Academic Editor: Sergey Leonov

Received: 11 November 2023
Revised: 25 December 2023
Accepted: 26 December 2023
Published: 28 December 2023

1. Introduction

The broad utilization of gas turbine engines is highly advantageous, and their thrust–weight ratio and thermal efficiency are significantly affected by the turbine inlet temperature, which has exceeded 2000 K. For the purposes of reducing the thermal loading of the gas turbine blades and extending their lifetime, protection of the turbine blades against extremely hot gases is typically carried out via film cooling. The extraction of coolant from the compressor is undertaken in the film cooling, followed by the injection of coolant into the hot gas on the blade surface, and the interaction of the coolant with the hot gas is made, which may lead to the formation of complicated vortex structures. Hence, the film cooling is a convective heat transfer problem dominated by the vortex structures. In particular, the major counter-rotating vortex pair (CRVP) lifts the coolant off the wall surface and entrains the hot gas beneath the coolant, resulting in a great reduction in the film cooling efficiency. Therefore, improving the film cooling efficiency through controlling the vortex structures of the film cooling is crucial for gas turbine engines.

Researchers have proposed various approaches to improve the film cooling efficiency, and the shaped film cooling hole is one of the effective approaches. Goldstein et al. [1]

originally found that the film cooling efficiency could be noticeably improved using fan-shaped holes, which could enhance the adherence and the lateral coverage of the coolant. Thereafter, numerous scholars concentrated on the shaped holes and proposed various shaped holes. Later, Bunker et al. [2] reviewed the origins of the classical shaped film cooling holes, summarized our knowledge of the shaped film cooling holes, and demonstrated that the shaped film cooling holes also have some drawbacks (e.g., high aerodynamic mixing losses). Recently, Saumweber et al. [3] attempted to further figure out the effects of the inclination angle, expansion angle, and length of the inlet cylindrical section on the film cooling efficiency of the fan-shaped holes and reported that the changes in geometrical parameters could significantly affect the film cooling efficiency. Except for the shaped film cooling holes, auxiliary regulating devices were proposed to weaken the destructive features of the vortex structures for enhancing the film cooling efficiency. Kusterer et al. [4] invented double-jet holes with compound angles to improve the film cooling efficiency, and it was revealed that the CRVPs of the double-jet hole mutually interfered with and counteracted each other, thereby enhancing the film cooling efficiency, while the double-jet holes required a reasonable arrangement. A ramped vortex generator was placed downstream of the cooling hole for terminating the CRVP progression via creating a new vortex pair; thus, the coolant was positioned close to the wall surface and stretched further downstream [5]. Recently, the film cooling performance (FCP) of a novel furcate hole was examined, and it was found that the lateral coverage of the coolant was more comprehensive than that of the traditional cylindrical holes [6]. Generally, all of the aforementioned approaches are passive flow control techniques and are limited, and the dynamic nature of the film cooling flow requires a flow control technique, which could be adjusted in real-time in the course of the flow state, emphasizing the demand for an active film cooling control technique.

Scholars have proposed pulsed film cooling to optimize the film cooling efficiency. Ekkad et al. [7] firstly used solenoid valves to directly control the cooling jet for improving the film cooling efficiency and found that the effects of pulsed jets on the film cooling showed promising outcomes. Thereafter, the film cooling efficiency and flow field temperature were examined at different BRs for a variety of pulsing frequencies and duty cycles, and it was revealed that pulsing at high frequencies was beneficial to reduce the overall jet lift-off in some cases, thereby improving the film cooling efficiency, whereas pulsing at low frequencies tended to produce the opposite effect [8]. The influences of the duty cycle and Strouhal number on the pulsed film cooling efficiency, particularly at high BRs, were numerically figured out [9], and it was noted that the recirculation region downstream of the cooling hole was remarkably reduced with pulsing, leading to an increment in the film cooling efficiency. Rutledge et al. [10] analyzed the influences of the pulsed film cooling on the turbine blade heat flux, and the superiority of steady film cooling to pulsed film cooling at a low BR was confirmed, while pulsed film cooling could be beneficial at a high BR, confirming the flat plate film cooling. The LES was employed to indicate how the square-wave pulsating film cooling jet could be interacted with recirculation vortexes, and the noticeable role of entraining recirculation vortexes in the near-wall region was figured out [11]. In recent years, coolant pulsation, as one of the active control techniques, has exhibited a high degree of efficiency that could improve the film cooling efficiency; however, further conclusive outcomes are essential [12] and evidence is required to prove the role of coolant pulsation in enhancing the film cooling efficiency. It is worth noting that hot gas unsteadiness will inevitably cause coolant pulsation in real engines, and the large-scale vortex structures of the pulsed film cooling are more complicated than those of the steady film cooling. Therefore, exploring active flow control techniques to effectively improve the pulsed film cooling efficiency may be advantageous for gas turbine engines.

The DBDPA has been successfully applied in numerous fields [13,14]. Benmoussa conducted a comprehensive exploration of the influence of dielectric barrier discharge plasma actuators (DBDPAs) on the entire spatial–temporal development (STD) of the flow field in quiescent air [15]. In a subsequent study by Benmoussa et al. [16], the investigation delved into the impact of DBD plasma actuators on the spatial–temporal development of the flow field in quiescent air. This research showcased the substantial influence of active flow control, emphasizing its significant role in enhancing the performance of cycloidal rotors. Daraee [17] numerically investigated the impact of plasma actuators on Vertical-Axis Wind Turbines (VAWTs), specifically focusing on optimizing installation positions and activation timings. The study unveiled a significant improvement in the turbine power coefficient through strategic actuator deployment. Yang et al. [18] assessed the influence of the DBDPA on the entire spatial–temporal development (STD) of the flow field in quiescent air. For the purpose of integrating the plasma and fluid dynamics, the phenomenological model and the first-principles-based model of the DBD were proposed, facilitating the integration of multi-dimensional plasma dynamics with fluid dynamics [19]. Singh et al. [20] investigated a plasma actuator's impact on spatial–temporal flow field development in quiescent air, revealing a fourth-order polynomial relationship between the induced fluid velocity and the amplitude of the rf potential. Researchers have proposed various plasma models to estimate electric fluid dynamics, including algebraic models and chemical models [21]. Chemical models take into account the plasma's chemistry, which involves various ions, electrons, and neutral substances. The equations in chemical models are computationally expensive due to the need to solve the dynamic control equations of ionized air substances for inferring electric dynamics. Thus, the phenomenological model appears to be highly advantageous. Hence, Roy and Wang [22] first utilized the DBD PAA to improve the film cooling efficiency, and the numerical findings revealed the active alteration of flow structures by the plasma aerodynamics near the DBDPA, thereby inducing the attachment of the coolant to the wall surface. Later, He et al. [23–25] further investigated the effects of the position, power input, number, and geometry of the DBDPA on the FCP, providing a deeper understanding of the mechanism of the PAA for improving the film cooling efficiency. Recently, Dolati et al. [26] employed neural networks to generalize the complicated communication that involves variables (e.g., flow, geometric, and electrical variables), thus gaining a useful correlation with different input–output parameters. Accordingly, Audier et al. [27] explored the ability of the PAA for the film cooling efficiency's enhancement through an experimental setup, and the experimental results confirmed the advantages of the PAA for improving the film cooling efficiency as predicted by the abovementioned numerical findings. More recently, it was demonstrated that the PAA could actively control large-scale coherent structures (LSCSs) of film cooling, and the coherent structures were reduced in size and number, making them beneficial for film cooling [28,29]. In general, the promising potential of the PAA for the film cooling efficiency's enhancement has been well demonstrated both numerically and experimentally. However, it is essential to indicate how the PAA can control pulsed film cooling.

The impact of dielectric barrier discharge (DBD) plasma on the temperature field remains a subject of significant controversy. Experimental measurements performed by Jukes et al. [30] revealed a modest temperature change of only 2 °C near the metal electrodes of the DBD plasma exciter. This led to the conclusion that the aerodynamic excitation induced by plasma has a negligible effect on the temperature field. In a numerical study aimed at improving the film cooling efficiency using DBD plasma aerodynamic excitation, Liming He et al. from the Air Force Engineering University [31] considered the heat generated by the exciter. They found that, although the exciter converted some electrical energy into heat, the impact on the overall film cooling effect was minimal due to the limited heat generated during ionization and the dissipation of heat by a large amount of upstream cooling airflow. Subsequent numerical studies by the research group [24] did not account for the heat generated by the plasma exciter in its influence on film cooling. Similarly, Roy and Wang [22] conducted a numerical study on the enhancement of the film cooling efficiency through plasma aerodynamic excitation without considering the heat produced by the exciter. Experimental results from Audier et al. [27] demonstrated that plasma aerodynamic excitation could enhance the efficiency of slot film cooling. However, in their experiments, they did not explicitly discuss the impact of the heat generated by the plasma exciter on film cooling. As such, this study will temporarily overlook the discussion of the impact of the heating effects generated by the plasma actuator on film cooling.

In the current study, the pulsed film cooling flow coupled with the PAA was simulated via LES, and we then comparatively assessed the time-averaged flow fields to reveal the comprehensive effects of the coolant pulsation and the PAA on the film cooling performance. Subsequently, the STD of the LSCSs was quantified to further describe how the coolant pulsation and the PAA could influence the coolant-gas interaction.

2. Computational Domain and Boundary Conditions (BCs)

On the basis of the research by Kohli and Sinha et al. [32,33], the computational domain of the present study was established. Figure 1 shows the computational domain of the film cooling and the arrangement of the DBDPA. The computational domain consists of a cooling hole (cooling hole diameter d = 12.5 mm), its length (5.2 d), the streamwise angle of the cooling hole (35°), and a crossflow channel. The height, width, and length of the crossflow channel are 10 d, 3 d, and 38.5 d, respectively. The cooling hole exit's trailing edge was considered in order to place the Cartesian coordinate system's origin, and the computational domain's streamwise, lateral, and normal directions are denoted by the x-, y-, and z-axis, respectively. The DBDPA was arranged just downstream of the cooling hole.

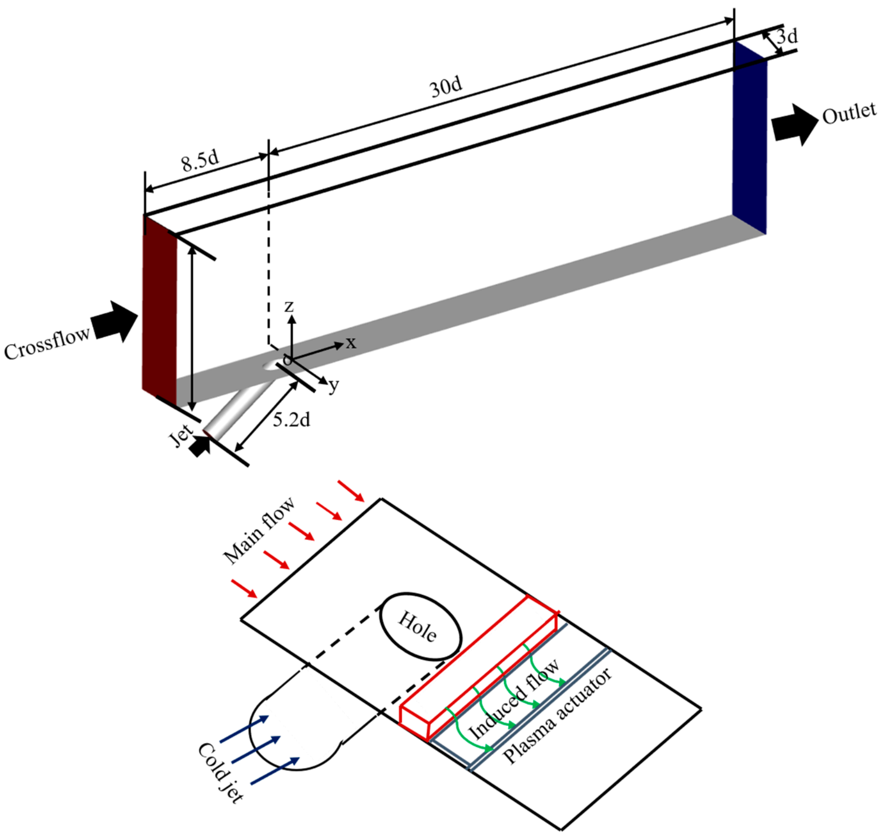

Figure 1. The physical model of flat plate film cooling.

The ANSYS CFD software was utilized for generating hexahedral meshes of the computational domain (Figure 2). The grid points are extremely refined near the walls of the flat plate and the cooling hole, and the y+ of the first layer mesh near the walls was less than 1.0. To avoid the generation of an excessive number of meshes, the stretching factor was about 1.05 in the wall-normal direction, and about 7 million meshes could be generated.

The BCs utilized in the current research are consistent with those presented in Kohli and Sinha et al.'s study [32,33], in which the crossflow atmosphere was ambient and the cooling jet was a mixture of CO_2 and N_2 at a temperature of 188 K. The velocity-inlet boundary was set at the inlet of the crossflow channel (crossflow velocity u_∞ = 20 m/s), temperature

(T_∞ = 298 K), and boundary layer thickness (δ = 1.0 d). We attempted to apply the pressure-outlet boundary at the outlet of the crossflow channel (static pressure, 101,325 Pa), Reynolds number (Re = $u_\infty d/v$ = 15,625), and kinematic viscosity ($v = 1.6 \times 10^{-5}$ m^2/s). The periodic conditions were set in the lateral direction of the crossflow channel (at $y/d = \pm 1.5$) for superimposing the influences of adjacent cooling jets. All walls were set to be adiabatic and non-slip.

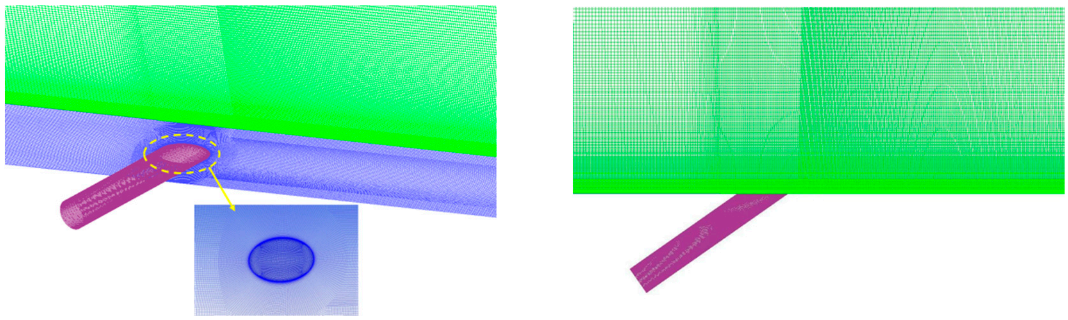

Figure 2. The meshing of the computational domain.

3. Governing Equations and Phenomenological Plasma Model

The LES can directly solve the LSCSs and simulate the sub-grid scale vortex structures via a sub-grid model approximately. Thus, the influences of the pulsation and the PAA on the LSCSs can be perfectly figured out, dominating the coolant–hot gas interaction. The algebraic wall-modeled LES (WMLES) model [34] was employed to assess the sub-grid scale dynamic effects, and the grid-filtered continuity, momentum, and energy equations for compressible flows can be formulated as

$$\frac{\partial \rho}{\partial t} + \frac{\partial}{\partial x_j}(\rho \overline{u_j}) = 0 \tag{1}$$

$$\frac{\partial}{\partial t}(\rho \overline{u_i}) + \frac{\partial}{\partial x_j}(\rho \overline{u_i u_j}) = \frac{\partial}{\partial x_j}(\sigma_{ij}) - \frac{\partial \overline{P}}{\partial x_i} - \frac{\partial \tau_{ij}}{\partial x_j} + F_i \tag{2}$$

$$\frac{\partial}{\partial t}(\rho \overline{E}) + \frac{\partial}{\partial x_j}(\rho \overline{u_j} \overline{E}) = -\frac{\partial \overline{p u_j}}{\partial x_j} + \frac{\partial}{\partial x_i} u_i(\sigma_{ij} - \tau_{ij}) - \frac{\partial}{\partial x_j}\left(\lambda \frac{\partial \overline{T}}{\partial x_j} - \frac{\rho v_{sgs}}{\mathrm{Pr}_{sgs}} \frac{\partial \overline{T}}{\partial x_j}\right) \tag{3}$$

In Equation (2), the sub-grid scale and viscous stress terms are defined as $\tau_{ij} = \rho \overline{u_i u_j} - \rho \overline{u_i}\,\overline{u_j}$ and $\sigma_{ij} = \left[\mu\left(\partial \overline{u_i}/\partial X_j + \partial \overline{u_j}/\partial X_i\right)\right] - 2/3\delta_{ij}\mu\left(\partial \overline{u_k}/\partial X_k\right)$ respectively. In Equation (3), the eddy viscosity is defined as $v_{sgs} = \min\left[(kd_w)^2, (C_{Smag}\Delta)^2\right] \cdot S \cdot \left\{1 - \exp\left[-(y^+/25)^3\right]\right\}$. More detailed parameters can be found in [34]. F_i is the EHD force vector generated by the DBDPA. We describe the phenomenological plasma model in the following sections.

A typical DBDPA is schematically illustrated in Figure 3. It consists of two electrodes insulated by a dielectric barrier and mounted on the wall surface. After applying a high alternating voltage to the exposed electrode, the nearby air is weakly ionized due to the barrier discharge, and a non-thermal plasma layer is generated over the covered electrode [35]. It was previously revealed that the EHD force generated by the DBDPA is the main mechanism of active flow control [36]. Shyy et al.'s phenomenological plasma model [37] was utilized to account for the EHD force, neglecting the momentum collision between the charged particles and the airflow. Hence, fewer computational resources are essential for this model, it can capture the main features of the plasma structure, and it has been successfully applied to diverse plasma-based flow control applications [38]. Film cooling flows were simulated via LES, which requires numerous computational resources, confirming the appropriateness of the phenomenological plasma model for solving for the EHD force [39]. The plasma occurs mainly in a tiny region just downstream of the exposed electrode and over the covered electrode (Figure 3a). Therefore, it was assumed that the DBDPA-generated EHD force acts on the airflow only in the triangular region ABC, whose height and length are denoted by a and b, respectively (Figure 3b). In our numerical simulations, the height of the plasma region was specified to be a = 2.0 mm in Equations (4) and (5), the width of the plasma region was denoted b = 4.0 mm, and the distance l was set to 0.25 mm. Point A is the location of the maximum electric field intensity ($E_0 = V_{pp}/l$), where l is the space between the two electrodes in the x-axis. A linear decrease in the electric field intensity is achievable with the movement from Source A, and the electric field intensity fluctuation can be formulated as

$$E = E_0 - k_1 x - k_2 z \tag{4}$$

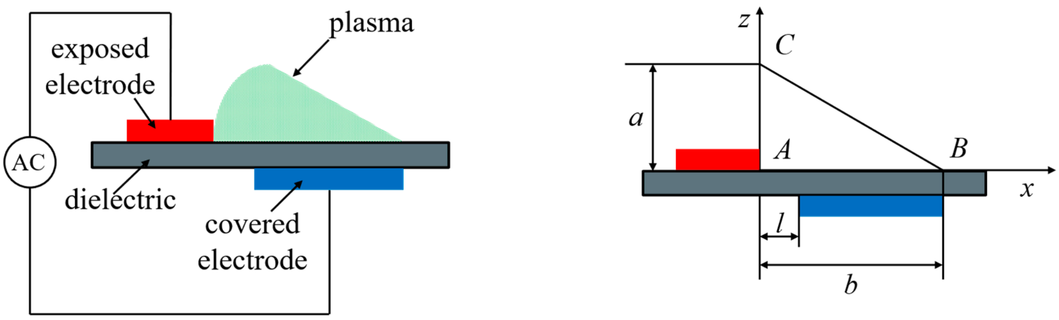

(**a**) Schematic illustration of the DBDPA (**b**) Geometry for the phenomenological plasma model

Figure 3. A schematic illustration of the DBDPA and the phenomenological plasma model.

In Equation (4), a field strength of E_b = 30 kV/cm was employed to assess $k_1 = (E_0 - E_b)/b$ and $k_2 = (E_0 - E_b)/a$ at the plasma boundary. Hence, the electric field intensity components in diverse directions are formulated as

$$E_z = Ek_1/\sqrt{k_1{}^2 + k_2{}^2}.\ E_x = Ek_2/\sqrt{k_1{}^2 + k_2{}^2} \tag{5}$$

The plasma discharge occurs at only one-half cycle and the time t_p is about 67 µs, during which the plasma forms. Thus, the EHD force components in the x and z directions can be formulated as

$$F_{ex} = \zeta \rho_e e E_x \vartheta t_p.\ F_{ez} = \zeta \rho_e e E_z \vartheta t_p \tag{6}$$

where $\rho_e = 10^{17}/\text{m}^3$ is the electron number density, e is the elementary charge, ϑ = 6.0 kHz is the frequency of the applied voltage, and ζ is the factor explaining the collision efficiency. A detailed explanation of the above values can be found in [37]. Additionally, it is crucial to note that the force is linearly attenuated along the internal normal direction of the triangular side, reaching its maximum value at the minimum gap between the plates. The high frequency of the plasma discharge (6.0 kHz) is correlative with the EHD force acting on the airflow as a constant; therefore, the DBDPA-generated EHD force was assumed to be a steady-state body force acting on the film cooling flow.

The ANSYS Fluent software was utilized for the LES of the pulsed film cooling flows with and without the DBDPA. The user-defined function (UDF) was employed to add EHD force components (i.e., body force terms) into the momentum equations, carrying the effects of the plasma discharge on the film cooling. The pressure interpolation was undertaken via the body force weighted scheme. The momentum and energy equations were solved discretely using a bounded central scheme and a second-order upwind scheme, respectively. The solvation of transient equations was carried out by the bounded second-order implicit scheme (time step, 1.0×10^{-5} s; maximum number of iterations, 40/time step). We considered a time-averaging approach, taking the main flow through the computational domain over a period ΔT = 0.017 s as one statistical cycle. Throughout this process, a total of 17,000 iterations were carried out, statistical averaging was performed over a duration of

$5 \times \Delta$T, and, in the current investigation, the CFL number was approximately 0.946. When a quasi-steady state could be reached by the film cooling flow, six cycles were allocated to the flow field to obtain time-averaged statistical information, in which the time of the crossflow through the crossflow channel was taken to be indicative of one cycle.

The adiabatic film cooling efficiency was formulated as

$$\eta(x/d, y/d) = (T_\infty - T_{\mathrm{aw}}(x/d, y/d))/(T_\infty - T_\mathrm{c}) \tag{7}$$

where T_{aw} is the temperature of the adiabatic wall. We attempted to average the adiabatic film cooling efficiency along the full lateral length in order to attain the lateral-averaged film cooling efficiency, which can be formulated as

$$\eta_{\mathrm{lat}} = \frac{1}{3}\int_{-1.5}^{1.5} \eta(x/d, y/d)d(y/d) \tag{8}$$

The UBL case is representative of un-pulsed film cooling flow, and the PBL-off case and the PBL-on case are indicative of pulsed film cooling flow without and with the DBDPA, respectively, in the current research.

The density ratio (DR) was equal to 1.6 ($\rho_\mathrm{c}/\rho_\infty$), the velocity-inlet boundary was applied at the inlet of the cooling hole, and the adjustment of the cooling jet inlet velocity was performed on the basis of the BR ($M = \rho_\mathrm{c} u_\mathrm{c}/\rho_\infty u_\infty$) and the momentum ratio $I = \rho_\mathrm{c} {u_\mathrm{c}}^2/\rho_\infty {u_\infty}^2$. For the un-pulsed film cooling, the BR was 1.0; thus, 12.5 m/s was allocated to the cooling jet velocity (u_c). For the pulsed film cooling, the total amount of the coolant was the same as for the steady film cooling in an operating cycle; thus, the time-averaged BR of the pulsed film cooling was 1.0 and the BR was in the range of 0.5–1.5 in a cycle (Figure 4). Therefore, the cooling jet velocity was specified as $u_\mathrm{c}(1.0 + 0.5\sin(2\pi ft))$, where f is the pulsation frequency of the cooling jet. The Strouhal number (St) of the coolant pulsation was defined as $St = df/u_\infty$, and St was set to 0.25.

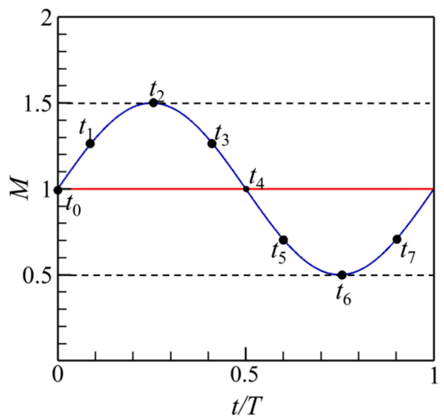

Figure 4. The BR variations of the pulsed and un-pulsed film cooling.

The asymmetric installation of the DBDPA was carried out downstream of the cooling hole exit (x/d = 0.0). The widths of the exposed electrode and covered electrode were 5 and 10 mm, respectively, l = 0.25 mm is indicative of the gap between the two electrodes, and a noticeable number of polyimide films were involved in the dielectric barrier. The length of the two electrodes was set to 3 d to avoid a restriction on the plasma generation in the lateral direction. The power supply of the DBDPA had a high frequency (6.0 kHz) and a high voltage (8.0 kVpp); thus, the electrohydrodynamic (EHD) force was estimated to be about 2 MN/m^3, which is compatible with the previously achieved value [18,19], and the power consumption of the plasma actuator was around 0.75 watts. However, it is worth noting that DBD plasma actuators are characterized by a low efficiency of electrical-to-fluid energy conversion, with a maximum efficiency below 0.1%. This efficiency is significantly lower than that of the other control devices we studied. Nevertheless, DBD plasma actuators offer such advantages as simplicity, a lack of moving parts, and a wide frequency band, making them suitable for practical flow control applications.

4. Model Validation

In order to verify the reliability of the phenomenological model used in the present study, the streamwise velocity profile of the numerical simulation results was compared with the results of Shyy et al. [37]. Figure 5 shows that, from the comparison of the numerical streamwise velocity and the experimental data, the maximum value of the streamwise velocity predicted by the phenomenological model agrees well with the experimental data and the vertical perturbation range affected by the DBD plasma is about 3 mm, which is in good agreement with the experimental measurement. Therefore, the phenomenological model used in the present study can effectively predict the influences of the DBDPA on the flow field.

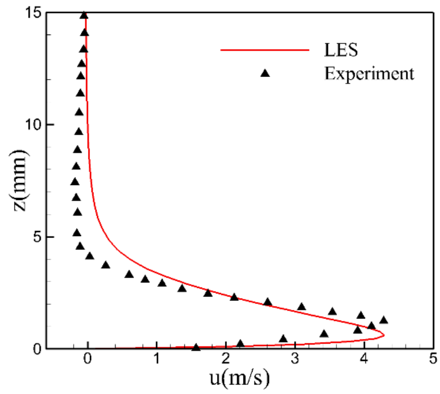

Figure 5. The flow induced by the DBDPA [29,37].

To validate the LES calculation procedure used in the present study, the centerline film cooling efficiency predicted by the LES was compared with the experimental results of Kohli and Sinha [32,33]. Figure 6 shows the LES predictions and experimental measurements of the centerline film cooling efficiency in the streamwise direction. It is apparent that the streamwise variations in the centerline film cooling efficiency show good agreement between the LES results and the experimental data, and there are some discrepancies downstream at $3 < x/d < 5$, where the recirculation region has formed and the reverse flow is complicated. This may be explained by the fact that the computational domain of the LES has no plenum and the cooling hole length is slightly longer than that in the experiments. Therefore, the LES calculation procedure used in the present study is feasible and acceptable. When using 6 million grids and 7 million grids, the differences between the two are negligible, and they align well with experimental data. Therefore, it can be considered that the numerical model constructed with 7 million grids provides a relatively accurate simulation of the original experimental model. In the subsequent computational processes, a numerical model with 7 million grids was employed.

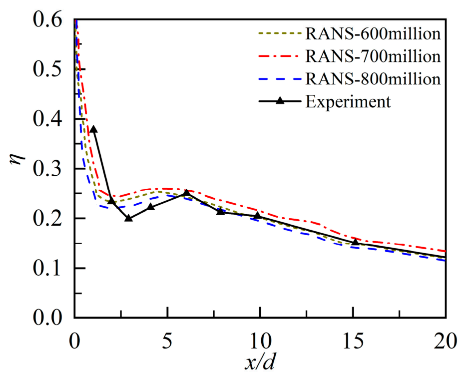

Figure 6. Comparison of centerline film cooling efficiency values.

5. Results and Discussion

5.1. Time-Averaged Flow Fields

The penetration extent of the cooling jet into the crossflow can be directly described by the jet trajectory, which is important to understanding the film cooling. Jet trajectories refer to a time-averaged streamline that may emanate from the center of the cooling hole exit (Figure 7). In the vicinity of the cooling hole, the same path of jet trajectories could be attributable to the high cooling jet exit momentum. While approaching downstream, momentum is gradually lost by the cooling jet, followed by a deflection in the downstream direction because of the pressure difference in the windward and leeward directions. At the trailing edge of the cooling hole exit, the PBL-off case exhibits a taller jet trajectory height versus the UBL case, which presumably results from the pulsed cooling jet's larger exit momentum at some times in the cycle, yielding adverse effects on the film cooling performance. Conversely, downstream at $x/d > 3$, the jet trajectory height of the PBL-off case is lower than that of the UBL case, which may be due to the fact that the pulsed cooling jet aggravates the mixing of the coolant with the crossflow. More importantly, compared with the other two cases, it is apparent that the jet trajectory height of the PBL-on case is remarkably shorter, demonstrating the improvement of the adherence of the coolant to the wall surface by the PAA.

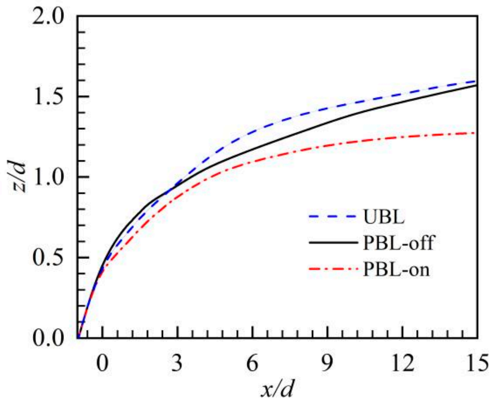

Figure 7. Jet trajectories.

At the cooling hole exit, time-averaged velocity profiles are illustrated in Figure 8. Once the crossflow is approached, the hole exit's velocity profile is affected, so the maximum values of the streamwise and normal velocities are shifted to the trailing edge of the hole exit. Near the trailing edge, the streamwise velocity of the PBL-off case was remarkably greater than that of the UBL case (Figure 8a), positively influencing the streamwise coverage of the coolant. Furthermore, the streamwise velocity became higher, which can be attributed to the PAA. Downstream of the cooling hole, the streamwise velocity of the UBL case and the PBL-off case is negative, implying that a recirculation zone has formed here. In the PBL-on case, the increase in the streamwise velocity can be attributed to the PAA. Near the trailing edge, compared with the UBL case, a noticeably higher normal velocity of the PBL-off case can be found (Figure 8b). This aggravates the interaction of the cooling jet with the crossflow, and the normal velocity has opposite characteristics near the leading edge. Moreover, compared with the PBL-off case, a noticeably higher normal velocity of the PBL-on case can be noted, which can be attributed to the PAA-generated downward force.

The profiles of the time-averaged streamwise velocity (u) at different values of x/d and y/d are illustrated in Figure 9. Downstream of the cooling at $x/d = 0.5$, there were negative values of the streamwise velocity in the near-wall region for the UBL case, reflecting detachment of the cooling jet from the wall surface and the formation of a recirculation region that would be immediately downstream of the cooling hole. For the PBL-off case, the negative values were slightly decreased due to the coolant pulsation. For the PBL-on case, the streamwise velocity values increased from negative to positive owing to the streamwise momentum injection effects generated by the PAA. This indicates that the recirculation region disappeared. Further downstream at x/d = 0.5, the streamwise velocity in the near-wall region was positive and large, signifying that the cooling jets had already reattached to the wall surface. Moreover, the streamwise velocity values of the PBL-on case are significantly larger than those of other two cases thanks to the PAA, showing that the PAA helps the coolant extend further downstream. While approaching downstream, the streamwise velocity values of the three cases become closer. This is due to the fact that the influences of the coolant pulsation and the PAA become weaker.

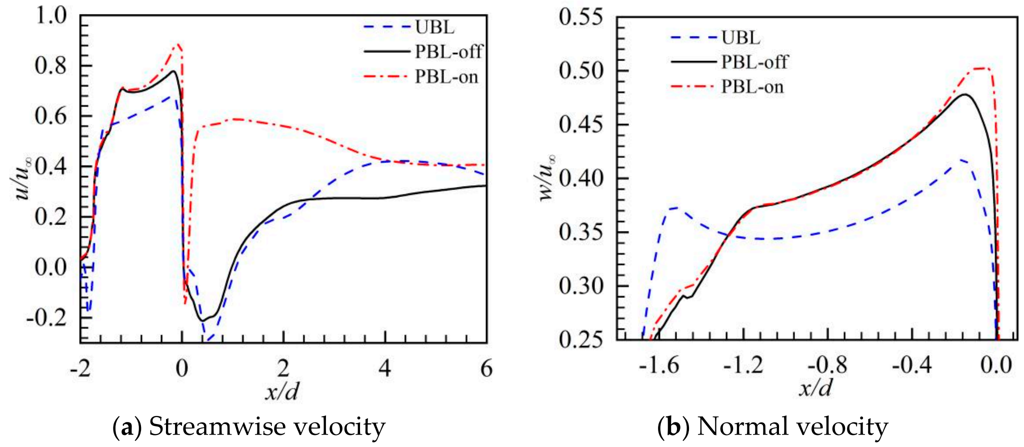

Figure 8. Time-averaged velocity profiles at the cooling hole exit (y/d = 0, z/d = 0.015).

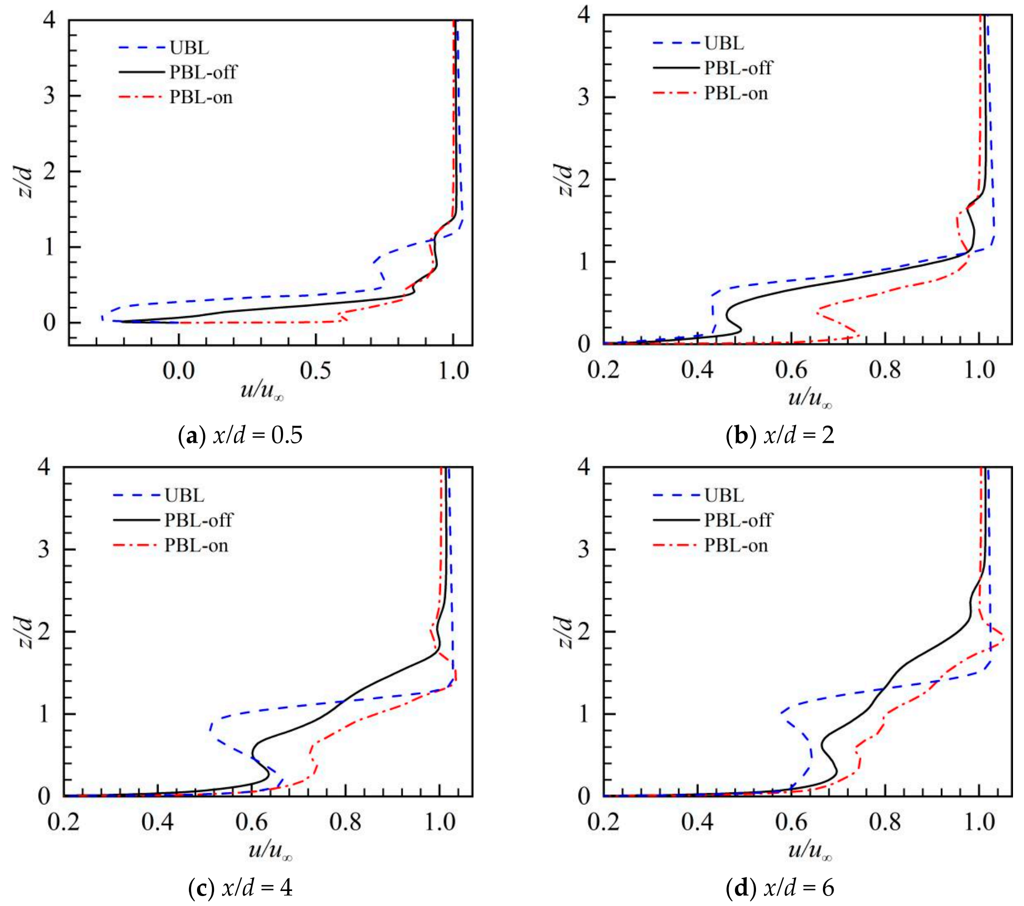

Figure 9. The profiles of the time-averaged streamwise velocity in the y/d = 0 plane.

Figure 10 shows the profiles of the time-averaged lateral velocity (v) at different values of (x/d, z/d). At x/d = 0.5, in the UBL case, the lateral velocity was negative and large, highlighting that the hot crossflow moves inward in the lateral direction and suppresses the lateral coverage of the coolant. This resulted from the entrainments of the CRVP. In the PBL-off case, the lateral velocity was decreased due to the coolant pulsation, which is beneficial to the lateral coverage of the coolant. In the PBL-on case, the lateral velocity had been significantly decreased owing to the PAA. This demonstrates that the PAA weakens the entrainments of the CRVP. Importantly, the absolute values of the lateral velocity became smaller while propagating downstream, highlighting that the vortex structures lost their strength and the effects of the PAA became weak. Downstream at x/d = 4 and x/d = 4, there was a narrower range of positive lateral velocities in the PBL-off case. This may have resulted from the fact that the pulsed cooling jet enlarges the horseshoe vortex, which drives the coolant flowing outward in the lateral direction. Under the influence of the PAA, there is a wide range of positive lateral velocities in the PBL-on case, meaning that the coolant slightly flows outward in the lateral direction and enlarges the lateral coverage of the coolant.

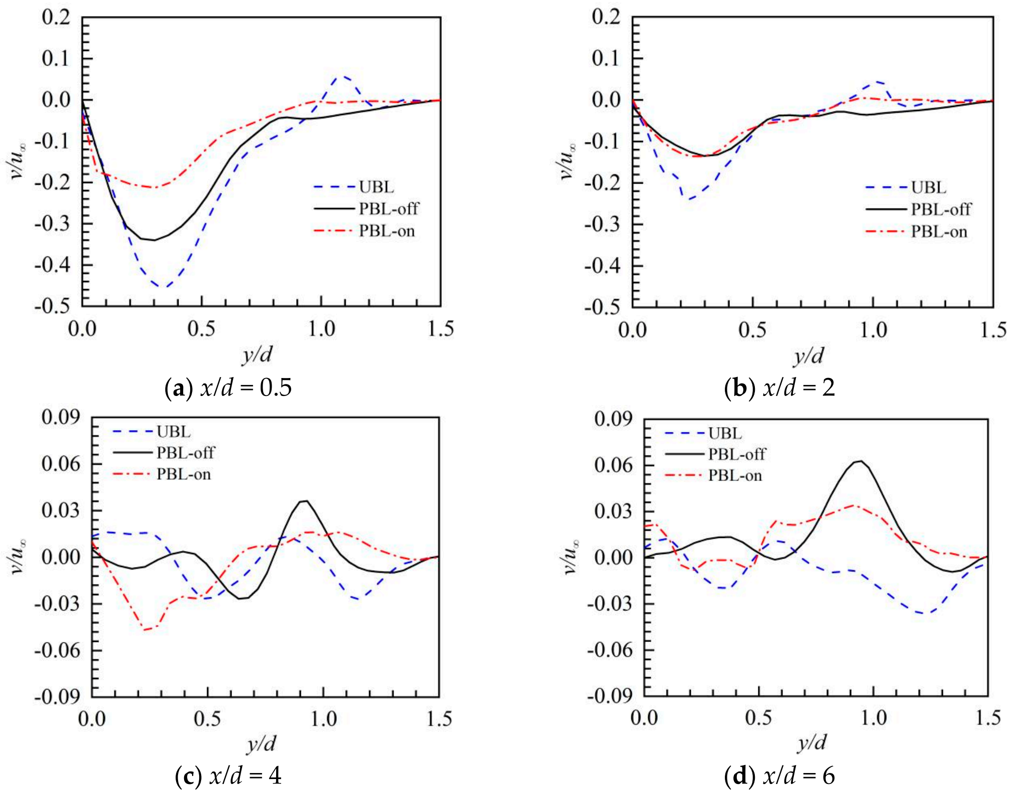

Figure 10. The profiles of time-averaged lateral velocity in the lateral direction.

Figures 11 and 12 illustrate the evolutions of the vortex structures and the temperature fields downstream of the cooling hole. At x/d = 1, a symmetrical CRVP can clearly be observed in the UBL case (Figure 11), followed by the entraining of the crossflow by the CRVP underneath the cooling jet and the lifting of the cooling jet off the wall, thereby negatively influencing the film cooling performance. Consequently, the high-temperature region rises upward at the midspan due to the upwash effects of the CRVP (Figure 12). In the PBL-off case, the influence region of the CRVP is larger than that of the UBL case since the coolant pulsation intensifies the interaction of the cooling jet with the crossflow and the core region of the cooling jet is enlarged (Figure 12). In the PBL-on case, the influence region of the CRVP is further enlarged, which is probably due to the momentum injection effects of the PAA. At x/d = 1, in the UBL case, a very small vortex pair (a horseshoe vortex) can be found in the near-wall region rotating in the opposite direction to the CRVP and delivering the coolant to the wall, thereby positively influencing the film cooling performance. In the PBL-off and PBL-on cases, there is no small vortex pair in the near-wall region. While evolving downstream, the CRVP gradually grows in structural size and moves away from the wall. Consequently, shifting of the low-temperature core region of the cooling jet away from the wall occurs (Figure 12), yielding a lower film cooling efficiency. Further downstream at x/d = 4, a small-scale horseshoe vortex can also be observed in the PBL-off and PBL-on cases, and the horseshoe vortex structural size of the PBL-off case is larger than that of the other two cases. This explains why there is a narrow positive lateral value in Figure 10. Furthermore, in the UBL case, in the near-wall region, there is a very small new vortex pair (i.e., a wall vortex). This can be attributed to the flow entrainment induced by the wall jet, and the lateral spreading of the coolant is promoted. At x/d = 6, a wall vortex is formed beneath the cooling jet in the PBL-off case, and the structural size of the horseshoe vortex is enlarged in the PBL-on case. These are both beneficial to the lateral coverage of the coolant. Compared with the PBL-off case, a reduction in the height of the low-temperature region can be noted in the PBL-off case (Figure 12), which could be attributable to the PAA-generated downward force. In addition, the core region of the cooling jet tends to split into two regions, and the CRVP-held region is gradually moving away from the wall, where the remarkable coolant–crossflow interaction occurs, resulting in the elevation of the temperature. The NWR is affected by the horseshoe vortex and the wall vortex, where the coolant stays close to the wall surface. The PAA not only weakens the lift-off effect of the CRVP but also helps the lateral coverage of the coolant; thus, the cooling jet was positioned closer to the wall surface and the lateral wall coverage of the low-temperature region was enlarged (Figure 12).

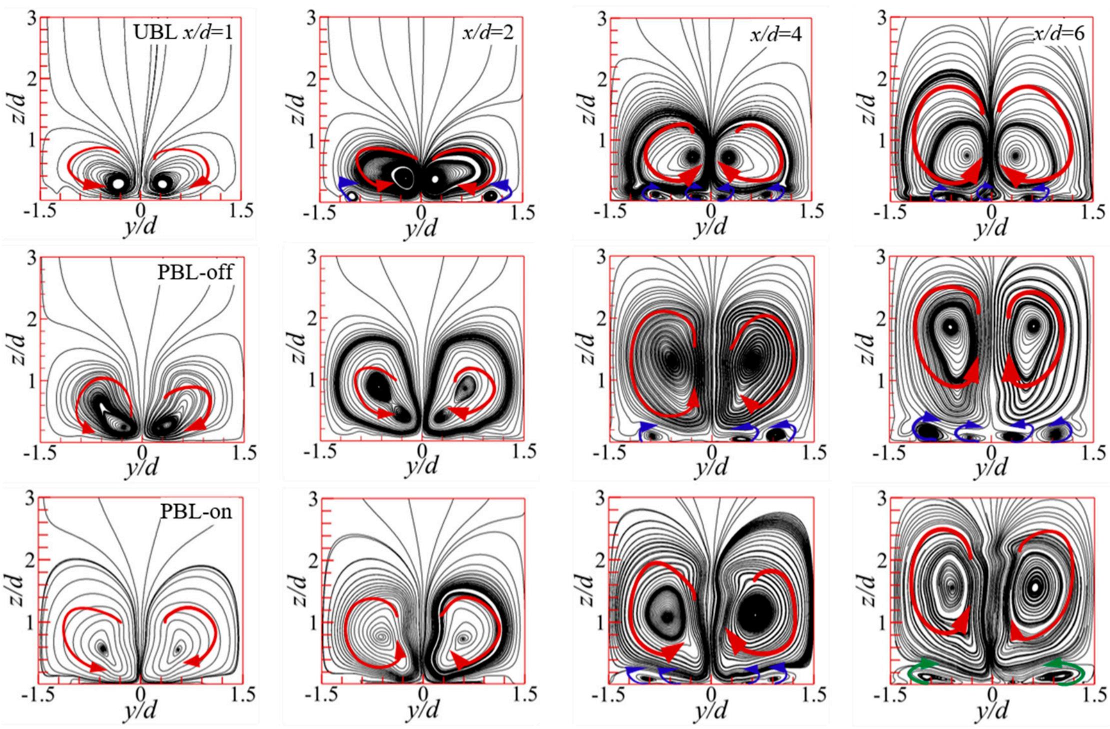

Figure 11. The time-averaged streamlines in the cross-sections downstream of the cooling hole.

On the wall surface, Figure 13 illustrates the contours of the time-averaged film cooling efficiency. For the UBL case, the FCE is fairly low just downstream of the cooling hole due to the blowing off of the cooling jet, then the film cooling efficiency rapidly increases thanks to the reattachment of the cooling jet. Thereafter, a gradual reduction in the film cooling efficiency can be noted while it approaches downstream as the coolant continually mixes with the crossflow. Compared with the UBL case, in the $2 < x/d < 6$ region, a reduction in the film cooling efficiency of the PBL-off case can be noted, indicating that the coolant pulsation aggravates the blowing-off effects and postpones the reattachment of the cooling jet. For the PBL-on case, a noticeable elevation in the film cooling efficiency can be found downstream of the cooling hole, which could be attributed to the PAA-generated momentum injection effect and the downward force suppressing the bowing-off of the cooling jet, thereby maintaining the coolant close to the wall surface. Because the PAA may inhibit the mixing of the coolant and the crossflow far downstream, a remarkably greater film cooling efficiency in the PBL-on case could be found compared with those of the other two cases.

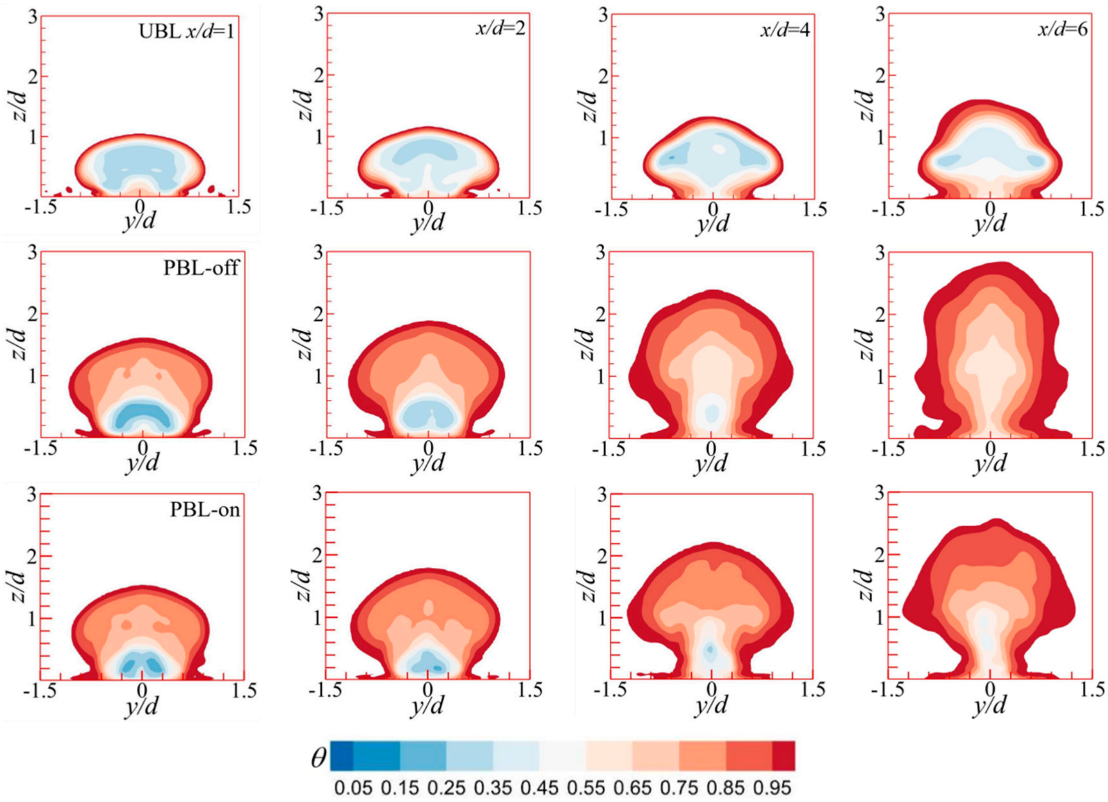

Figure 12. The contours of the time-averaged dimensionless temperature in the cross-sections downstream of the cooling hole.

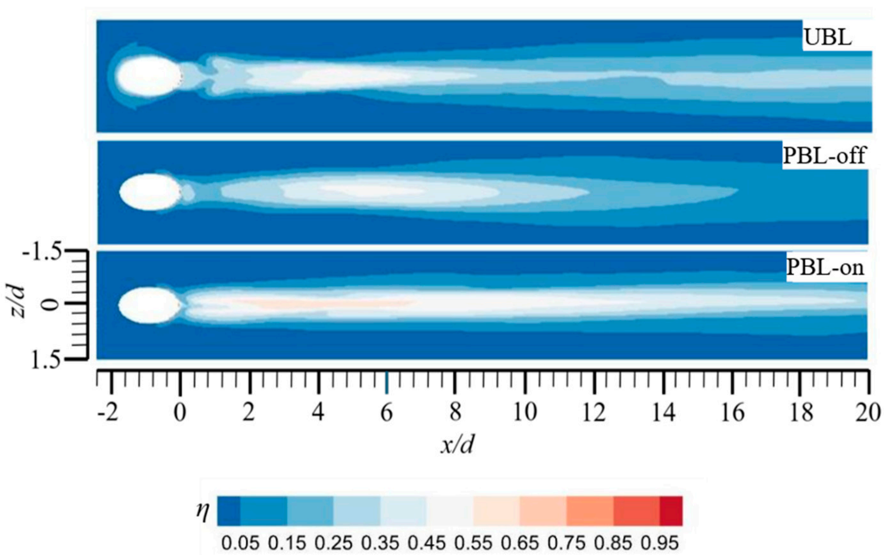

Figure 13. The contours of the time-averaged film cooling efficiency on the wall surface.

The flow structures can remarkably affect the film cooling efficiency in the near-wall region, and the time-averaged streamlines, especially on the wall surface, are illustrated in Figure 14. For the UBL case, a recirculation region can be found at the cooling hole just downstream, which could be attributed to the cooling jet's blocking influence and result in the formation of a downstream spiral separation node (DSSN) vortex pair. The DSSN vortex can exacerbate the mixing of the coolant with the cooling jet, yielding a lower film cooling efficiency (Figure 13). Then, due to the entrainment effect of the CRVP, most of the streamlines converge toward the centerline, which is detrimental to the lateral wall coverage of the coolant. A few streamlines diverged outward in a narrow region in the lateral direction as the beneficial effect of the wall vortex and the horseshoe vortex; however, this phenomenon disappeared quickly. For the PBL-off case, a recirculation region can also be clearly observed and the distributions of the streamlines are similar to the UBL case, while the tendency of the streamlines to converge is weaker than that of the UBL case. For the PBL-on case, there is no recirculation region downstream of the cooling hole because of the PAA-induced momentum injection effect, the streamlines converge rapidly toward the centerline, and the streamlines diverge outward while moving downstream, thus improving the lateral coverage of the coolant. This implies that the PAA weakens the detrimental entrainment effect of the CRVP.

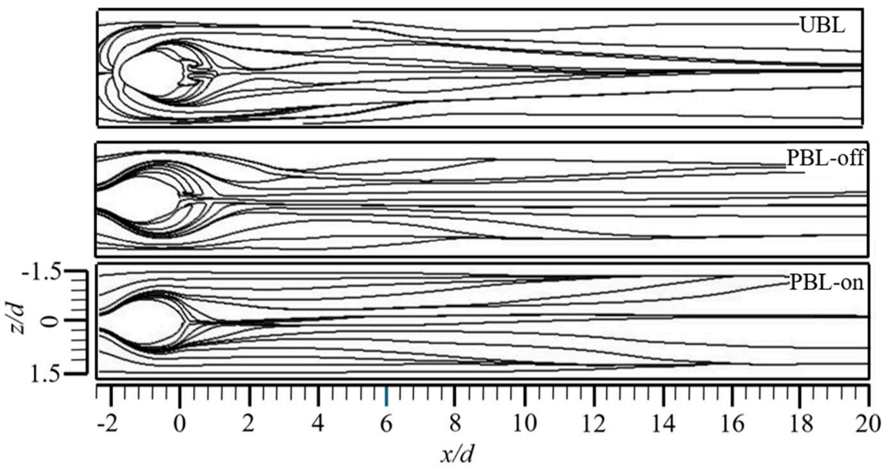

Figure 14. The time-averaged streamlines on the wall surface.

Figure 15 shows the distribution of the centerline and the lateral-averaged film cooling efficiency in the streamwise direction. As can be seen from Figure 15a, the centerline film cooling efficiency is very low due to the separation of the cooling jet. Then, the centerline film cooling efficiency quickly increases to the maximum value thanks to the reattachment of the cooling jet. Subsequently, the centerline film cooling efficiency continues in a gradual decline while evolving downstream due to the continual mixing of the coolant and the crossflow. For the PBL-off case, the centerline film cooling efficiency just downstream of the cooling hole is lower than that of the UBL case and the streamwise location of the maximum value has shifted downstream, which may have resulted from the reduction in the adherence of the coolant. For the PBL-on case, the centerline film cooling efficiency has been significantly increased and the streamwise location of the maximum value has shifted upstream. In the UBL case, the lateral-averaged film cooling efficiency is the lowest in the recirculation region and then gradually rises while propagating downstream, which is different from the centerline film cooling efficiency (Figure 15b). However, in the PBL-off case, there is a degree of similarity in the tendency of the lateral-averaged film cooling efficiency compared with the centerline film cooling efficiency. In the PBL-on case, the prominent elevation in the lateral-averaged film cooling could be attributable to the PAA, confirming the results illustrated in Figure 13, and the continuous increase in the lateral-averaged film cooling efficiency up to x/d >15 is noteworthy. When x/d >15, the lateral-averaged film cooling efficiency slightly decreases as it approaches downstream, which is probably because the coolant is already highly mixed with the crossflow. Generally, the PAA can effectively improve the pulsed film cooling efficiency. This is beneficial to controlling the pulsed film cooling flow caused by the unsteadiness in the main flow in actual engines.

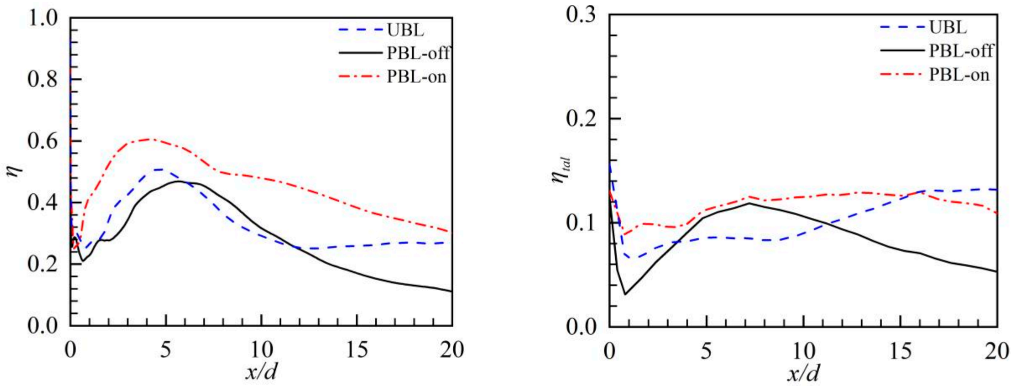

(**a**) Centerline cooling efficiency (**b**) Lateral−averaged cooling efficiency

Figure 15. The distribution of the film cooling efficiency in the streamwise direction.

Figure 16 presents a comparison of wall temperatures in the three different cases. From Figure 16, it is evident that the transition from steady film cooling to pulsed film cooling results in a slight decrease in the film cooling efficiency, a reduction of 15.1%. This underscores the significance of acknowledging that the unsteadiness in hot gas inevitably induces coolant pulsations in real engines. When employing the DBDPA, the wall-averaged film cooling efficiency increases to 13.5%. In comparison with the conditions without the DBDPA, the cooling efficiency experiences a substantial improvement of 42.1%. This enhancement is attributed to the momentum injection effect introduced by the DBDPA and the suppression of CRVP development, thereby significantly elevating the film cooling efficiency. In the following sections, we delve further into the mechanisms through which the DBDPA enhances the film cooling efficiency.

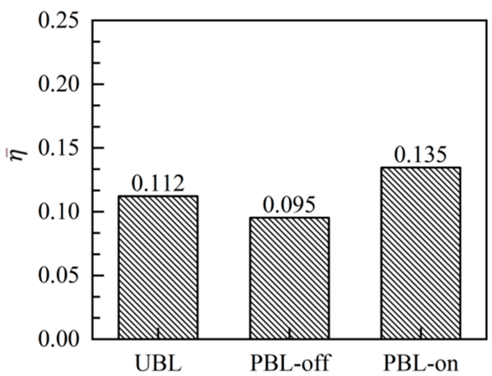

Figure 16. Comparing the wall-averaged film cooling efficiency.

5.2. Instantaneous Flow Fields

In order to comprehensively reveal the underlying mechanism of the coolant pulsation and the PAA for controlling the film cooling flow, the STD of coherent structures in the wake flow of the film cooling was comparatively analyzed. The identification of the coherent structures was undertaken using the Q-criterion method, which is defined as $Q = \left(\Omega_{ij}\Omega_{ij} - S_{ij}S_{ij}\right)/2$, where $\Omega_{ij} = \left(\partial u_i/\partial x_j - \partial u_j/\partial x_i\right)/2$ and $S_{ij} = \left(\partial u_i/\partial x_j + \partial u_j/\partial x_i\right)/2$ [40]. Eight time points were taken in a pulsation cycle to better interpret the cooling flow field (Figure 3).

The instantaneous Q iso-surface was colored by the dimensionless temperature (DT, θ), where DT (θ) = $(T - T_c)/(T_\infty - T_c)$ (Figures 17–19). In the UBL case, the classical coherent structures can be clearly observed. It can be seen that horseshoe vortices form upstream of the cooling hole exit due to the pressure gradient. The fluid temperature in the horseshoe vortices is higher, indicating the aggravation of the mixing of the coolant and the crossflow via the horseshoe vortices. Notably, a series of structurally complete hairpin vortices can be clearly identified, and these hairpin vortices actually dominate the entrainment and mixing of the crossflow. There is a close association of heads, normal legs, and horizontal legs of the hairpin vortices with a shear layer vortex, an upright wake vortex, and the CRVP, respectively [41]. The heads of the hairpin vortices are caused by a shearing effect that leads to a strong entrainment of the coolant with the crossflow. As a result, an increase in the mixed fluid temperature can be found around the heads of the hairpin vortices. An enlarged size of the hairpin vortices and their gradual shifting away from the wall can be found. Small-scale turbulent vortices eventually result, highlighting their noticeable role in the far-field region.

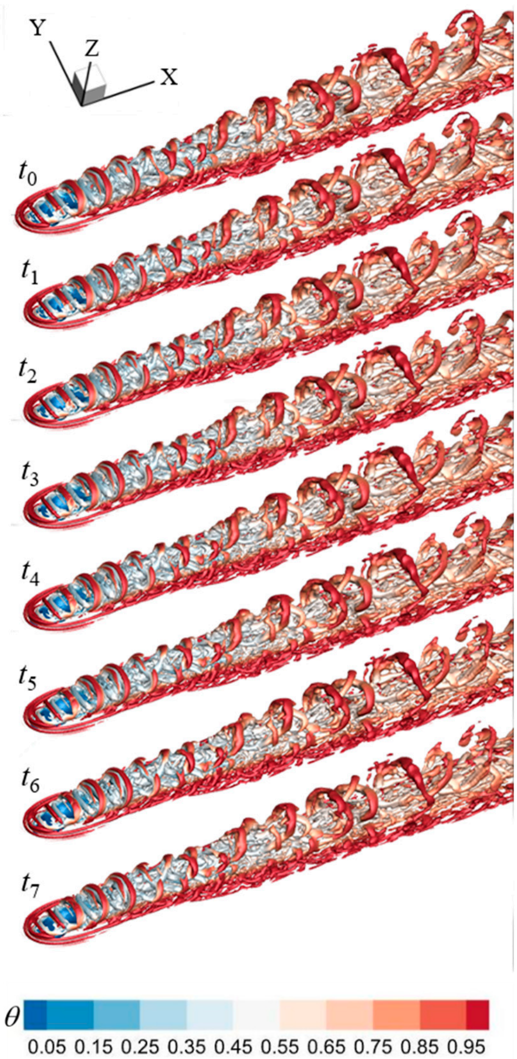

Figure 17. The instantaneous Q iso-surface colored by temperature in the UBL case ($Q = 5.0 \times 10^5$).

In the PBL-off case, horseshoe vortices are also found upstream of the cooling hole exit. Their structural sizes are smaller than those of the UBL case, and their structural sizes also varied with time due to the pulsation of the cooling jet. Notably, instead of structurally complete hairpin vortices, LSCSs are clearly observed, and these coherent structure groups are intermittently distributed in the wake region, which may have resulted from the periodic variations in the cooling jet–crossflow interaction, which is caused by the pulsation of the cooling jet. In the case of a noticeable BR, the cooling jet–crossflow interaction strongly forms coherent structure groups; conversely (i.e., a reduced BR), a close position of the cooling jet to the wall surface is expected. Moreover, the generation, development, stretching distortion, and breakup of the coherent structure groups can be clearly observed from $t = t_0$ to $t = t_7$. The coherent structure groups persist downstream over a short distance and happen to break up earlier, leading to a low film cooling efficiency in the wake region.

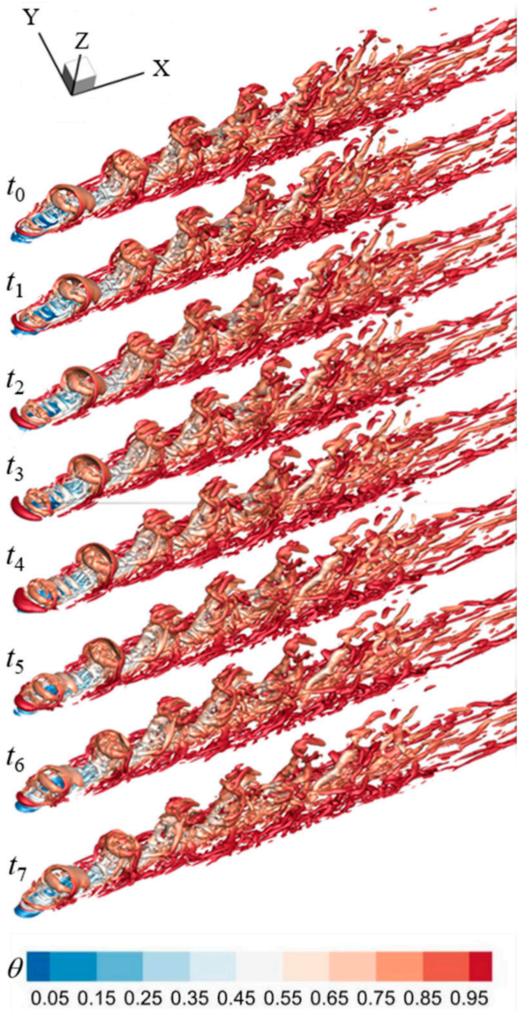

Figure 18. The instantaneous Q iso-surface colored by temperature in the PBL-off case ($Q = 5.0 \times 10^5$).

After applying the PAA (Figure 19), the structural sizes of the coherent structure groups are greatly reduced, and the number of LSCSs in the groups is also reduced. These variations may result from the PAA-generated downward force inhibiting the penetration of the pulsed cooling jet into the cooling flow, thereby weakening the pulsed jet–crossflow interaction. Moreover, the downward force causes the deflection of the pulsed cooling jet toward the wall surface, leading to the closer position of coherent structure groups relative to the wall surface. The intermittent coherent structure groups persist downstream over a shorter distance and happen to break up earlier than those in the PBL-off case. In addition, the turbulent vortices in the far-field region are smaller than those of the PBL-off case, thus reducing the turbulent incorporation of the crossflow into the coolant.

Coherent structures are beneficial to determining temperature distributions, especially in the flat plate, and the fluctuations in the DT, particularly in the hole centerline in a cycle, are illustrated in Figures 20–22. The fluctuation in the centerline temperature (CT) around the time-averaged values can be found in a cycle, while their distribution trends in the streamwise direction are likely to remain unchanged. In the UBL case, the fluctuation values of the CT are smaller than those of the other two cases because the un-pulsed film cooling has the same BR during a cycle. The small CT fluctuations are presumably caused by the spatial–temporal evolutions of the coherent structures, which are intermittently distributed in the wake region.

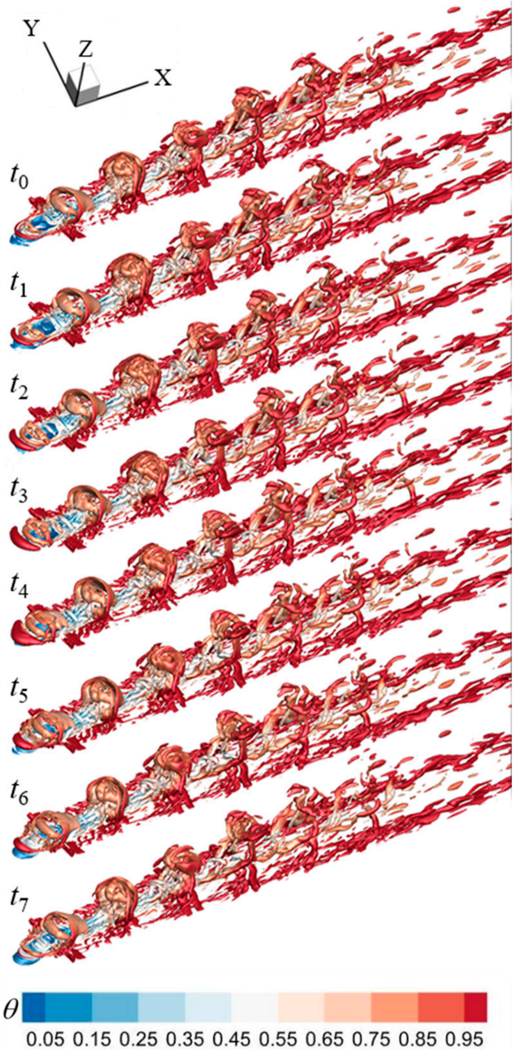

Figure 19. The instantaneous Q iso-surface colored by temperature in the PBL-on case ($Q = 5.0 \times 10^5$).

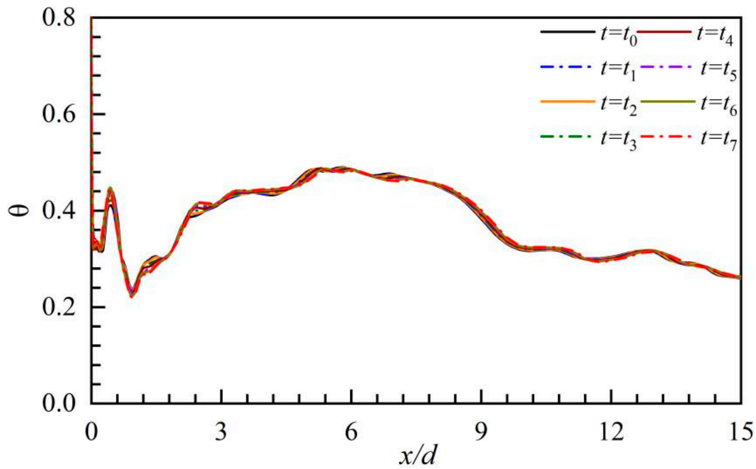

Figure 20. The variations in the DT on the hole centerline in the UBL case.

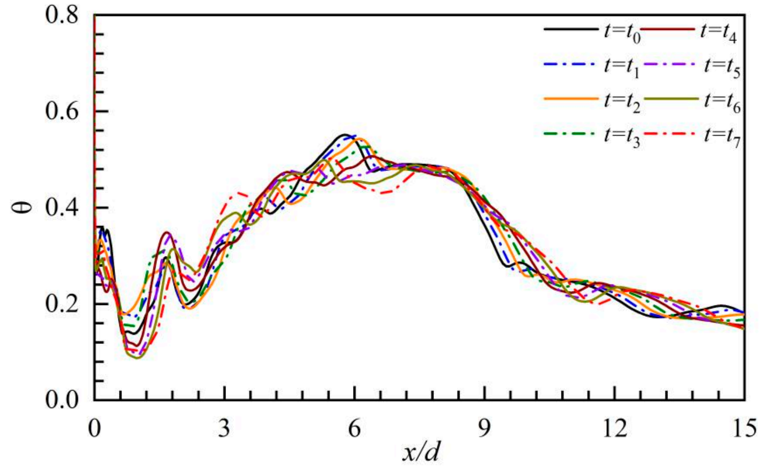

Figure 21. The variations in the DT on the hole centerline in the PBL-off case.

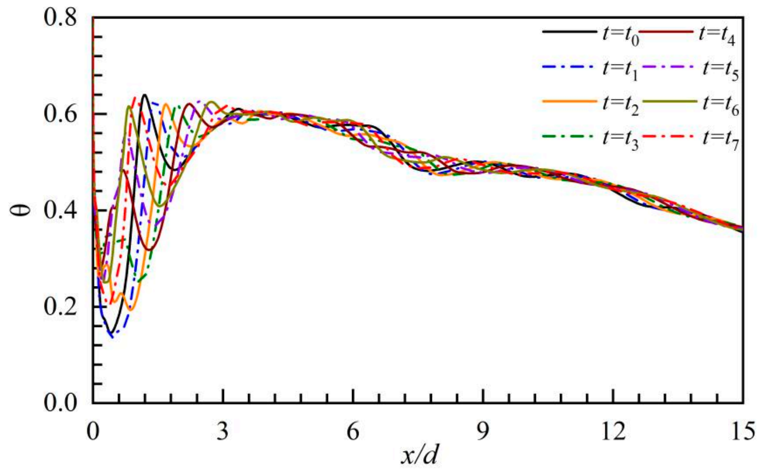

Figure 22. The variations in the DT on the hole centerline in the PBL-on case.

In the PBL-off case, the centerline DT varies regularly with time, and this is very different from the UBL case. The positions of the minimum CT values significantly fluctuate with time and may be located in the recirculation region where the reverse flow is fairly complicated due to the pulsed cooling jet. As time goes by, the intermittent coherent structure groups periodically approach downstream accompanied by the pulsed cooling jet flow, thus leading to the organized alterations in the CT. At $t = t_0$, the coherent structure groups happen to break up at $x/d = 6$, followed by turbulent incorporation of the coolant into the crossflow, which is remarkably enhanced, and a rapid increase in the CT. The last coherent structure group is regularly and gradually extended downstream, the locations of the minimal CT are accordingly altered downstream, and there is an increment in the minimum CT due to the turbulent incorporation effect. In the far-field region, the CT is also regularly altered with time as the small-scale turbulent vortices still propagate downstream in an orderly manner.

In the PBL-on case, the centerline DT is significantly lower than that of the PBL-off case. Clearly, the CT just downstream of the cooling hole remarkably fluctuates with time. This is because the PAA may effectively terminate the reverse flow just downstream of the cooling hole since the BR is low and the control effects of the PAA are reduced as the BR increases. At $x/d > 3$, compared with the PBL-off case, the fluctuations in the CT are noticeably lower because the PAA reduces the strength and size of the coherent structure groups.

Figure 23 shows the contours of the instantaneous DT in the $y/d = 0.0$ plane superimposed on the Q iso-surface, providing a new perspective on how the PAA affects the pulsed film cooling temperature field. In the UBL case, downstream of the cooling hole, the heads of the hairpin vortices cause strong entrainments and then aggravate the mixing of the coolant with the crossflow, thus resulting in billows at the interface of the cooling jet with the crossflow. It is reasonable to infer that the hairpin vortex head has detrimental effects on the film cooling performance. In the PBL-off case, the intermittent coherent structure groups dramatically aggravate the mixing of the coolant with the crossflow, resulting in the low-temperature regions outside of the wall surface. The low-temperature regions have obvious intermittency due to the pulsed cooling jet. In the PBL-on case, the structural sizes of the coherent structure groups are much smaller than those of the PBL-off case thanks to the PAA. As a result, the low-temperature regions stay closer to the wall surface, and the intermittency of the low-temperature regions is weakened.

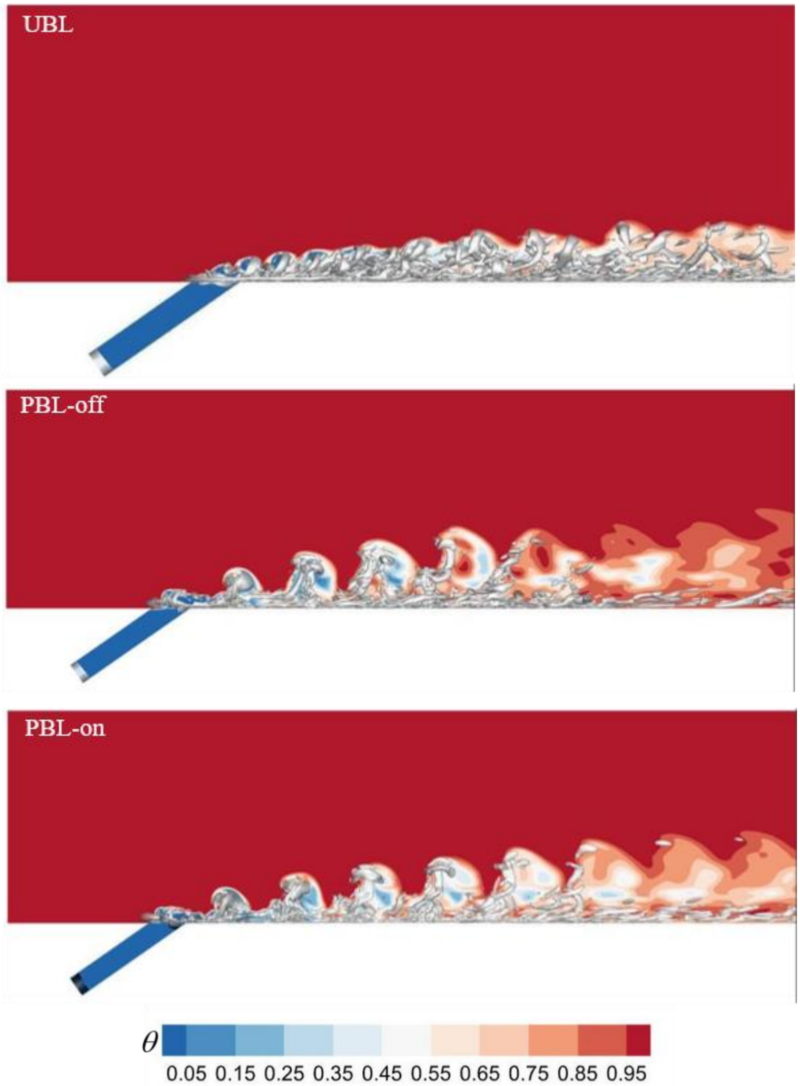

Figure 23. The contours of the instantaneous temperature in the z/d = 0.0 plane.

In order to deepen our comprehension of the jet–crossflow interactions, the three-dimensional streamlines are drawn in Figure 24. As can be seen from the purple streamlines, a horseshoe vortex forms upstream of the cooling hole exit. In the UBL case, the purple streamlines wrap around the cooling jet, flow into the recirculation region, exacerbate the turbulent mixing, and then eventually intertwine with the red streamlines and contribute to the development of the CRVP. While approaching downstream, the purple streamlines and the red streamlines gradually shift away from the wall together, accompanied by the cooling jet flow. In the PBL-off case, the purple streamlines have larger heights upstream of the cooling hole exit due to the higher instantaneous BR, meaning that the horseshoe vortex has higher strength. The majority of the purple streamlines flow directly downstream, and some of the purple streamlines intertwine with the red streamlines. Moreover, just downstream of the cooling hole exit, the red streamlines stay closer to the wall surface since the BR is low at this moment. Then, the red streamlines rapidly move away from the wall surface due to the coherent structure group. In the PBL-on case, the purple streamlines shift downstream, indicating that a horseshoe vortex formed slightly further downstream. This may have resulted from the PAA-generated downward force that may push the cooling jet closer to the wall surface, thereby attenuating the pressure gradient upstream of the cooling hole. Downstream of the cooling hole, the red streamlines and the purple streamlines are closer to the wall surface, indicating that the PAA weakens the lift-off effects of the CRVP.

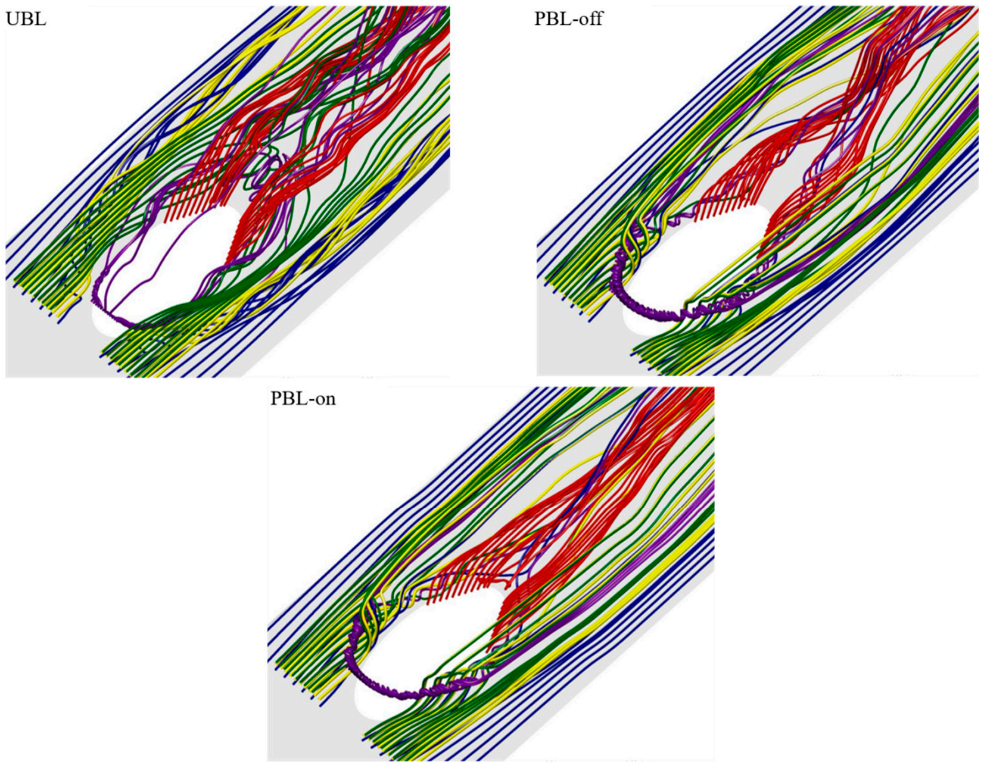

Figure 24. Interaction of the upstream flow with the jet and the crossflow at the same moment.

6. Conclusions

LESs of pulsed film cooling without and with the PAA were established to uncover the underlying control mechanisms. The time-averaged film cooling flow fields were studied qualitatively and quantitatively. Then, the spatial–temporal evolutions of the coherent structures were analyzed to figure out the influences more comprehensively. The main conclusions can be summarized as follows:

(1) The coolant pulsation might cause a slight reduction in the film cooling efficiency as the averaged pulsation BR was 1.0, while the PAA could effectively improve the pulsed film cooling efficiency and it would be superior to steady-state film cooling;

(2) The pulsed cooling jet can penetrate more deeply than steady-state film cooling in the near-hole region. Thus, the jet–crossflow interactions produced a large-scale CRVP, promoting the turbulent integration. Because of the downward force generated by the PAA, the penetration depth of the pulsed cooling jet was greatly reduced, which could be attributable to the downward force. The detrimental lift-off effect and entrainment of the CRVP were weakened.

(3) Rather than hairpin vortices, intermittent coherent structure groups formed in the pulsed film cooling, and these groups also had upcast behavior and moved away from the wall surface while evolving downstream, thereby aggravating the turbulent

integration of the coolant with the crossflow. The coherent structure groups were reduced in size and strength owing to the PAA, and their upcast behavior was attenuated; thus, the turbulent integration was suppressed and the film cooling efficiency was enhanced.

(4) The three-dimensional streamlines also confirmed that the PAA could effectively control the unsteady dynamic behavior of the LSCSs. The height of the three-dimensional streamlines was significantly reduced, indicating that the pulsed cooling jet flow was positioned close to the wall surface owing to the PAA.

(5) Operating with an AC voltage of V(t) = $V_{\max} \times \sin(2\text{ft})$, where $V_{\max}$ = 8 kV and f = 6 kHz, the PAA demonstrated compelling results. Importantly, the power supply characteristics (a high frequency of 6.0 kHz and a high voltage of 8.0 kVpp) translated into an estimated EHD force of about 2 MN/m3. Remarkably, the power consumption of the plasma actuator remained minimal, at approximately 0.75 watts.

Author Contributions: Conceptualization, G.L. and Z.S.; methodology, G.L.; software, B.H.; validation, Z.S., G.L. and H.Z.; formal analysis, Z.S. and G.L.; investigation, Z.S.; resources, B.H.; data curation, Z.S.; writing—original draft preparation, Z.S.; writing—review and editing, Z.S.; visualization, B.H.; supervision, G.L.; project administration, H.Z.; funding acquisition, G.L. All authors have read and agreed to the published version of the manuscript.

Funding: The National Natural Science Foundation of China (Grant No. 12002335), the China Postdoctoral Science Foundation (Grant No. 2022M720166), the Fundamental Research Funds for the Provincial Universities of Zhejiang (Grant No. 2021YW24), and the Natural Science Foundation of Zhejiang (Grant No. LQ20E060006).

Data Availability Statement: Data available on request from the authors. The data that support the findings of this study are available from the corresponding author, [Zhou Shen], upon reasonable request.

Acknowledgments: The authors gratefully acknowledge the financial support for this study from the National Natural Science Foundation of China (Grant No. 12002335), the China Postdoctoral Science Foundation (Grant No. 2022M720166), the Fundamental Research Funds for the Provincial Universities of Zhejiang (Grant No. 2021YW24), and the Natural Science Foundation of Zhejiang (Grant No. LQ20E060006).

Conflicts of Interest: The authors declare that they have no known competing financial interests or personal relationships that could have appeared to influence the work reported in this paper.

Nomenclature

E	electric field intensity (V/m)
E_b	breakdown electric field intensity (V/m)
E_0	electric field intensity at the tip (V/m)
E_s	electric field intensity at serrated edge (V/m)
V_0	peak AC voltage (V)
l	space between the two electrodes (m)
l_a	distance from the root (m)
f	pulsation frequency (Hz)
e	elementary charge (C)
Δt	space of time (s)
a	height of plasma region (m)
b	length of plasma region (m)
k	constants in plasma model (-)
d	diameter of film-cooling hole (m)
x, y, z	cartesian coordinates (m)
u, v, w	velocity component index (m/s)
T	local fluid temperature (K)
t	time (s)
$\mathrm{k}_1, \mathrm{k}_2$	constants in plasma model (-)

Greek symbols	
ρ	gas density (kg/m^3)
λ	wavelength of plasma actuator (m)
α	intersection angle of actuator (°)
β	angle of plasma force at the tip (°)
η	film cooling efficiency (-)
ζ	collision efficiency (-)
δ	thickness of boundary layer (m)
ν	kinematic viscosity (m^2/s)
ν_{sgs}	eddy viscosity (m^2/s)
ϑ	applied voltage frequency (Hz)
Subscripts	
aw	adiabatic wall
∞	crossflow
c	jet flow
lat	lateral-averaged cooling efficiency
p	plasma actuation in a cycle

References

1. Goldstein, R.J.; Eckert, E.R.G.; Burggraf, F. Effects of hole geometry and density on three-dimensional film cooling. *Int. J. Heat. Mass Transf.* **1974**, *17*, 595–607. [CrossRef]
2. Bunker, R.S. A review of shaped hole turbine film-cooling technology. *J. Heat Transf.* **2005**, *127*, 441–453. [CrossRef]
3. Saumweber, C.; Schulz, A. Effect of geometry variations on the cooling performance of fan-shaped cooling holes. *J. Turbomach.* **2012**, *134*, 061008. [CrossRef]
4. Kusterer, K.; Bohn, D.; Sugimoto, T.; Tanaka, R. Double-jet ejection of cooling air for impr-oved film-cooling. In Proceedings of the ASME Turbo Expo 2006: Power for Land, Sea, and Air, Barcelona, Spain, 8–11 May 2006. [CrossRef]
5. Shinn, A.F.; Vanka, S.P. Large eddy simulations of film-cooling flows with a micro-ramp vortex generator. *J. Turbomach.* **2013**, *135*, 011004. [CrossRef]
6. Liu, C.L.; Ye, L.; Zhang, F.; Huang, R.; Li, B. Film cooling performance evaluation of the furcate hole with cross-flow coolant injection: A comparative study. *Int. J. Heat Mass Transf.* **2021**, *164*, 120457. [CrossRef]
7. Ekkad, S.V.; Ou, S.; Rivir, R.B. Effect of jet pulsation and duty cycle on film cooling from a single jet on a leading edge model. In Proceedings of the ASME Turbo Expo 2004: Power for Land, Sea, and Air, Vienna, Austria, 14–17 June 2004. ASME Paper No. IMECE 2004-60466. [CrossRef]
8. Coulthard, S.M.; Volino, R.J.; Flack, K.A. Effect of jet pulsing on film cooling—Part I: Effectiveness and flow-field temperature results. *J. Turbomach.* **2007**, *129*, 232–246. [CrossRef]
9. Muldoon, F.; Acharya, S. DNS study of pulsed film cooling for enhanced cooling effecti- veness. *Int. J. Heat Mass Transf.* **2009**, *52*, 3118–3127. [CrossRef]
10. Rutledge, J.L.; King, P.I.; Rivir, R.B. Influence of film cooling unsteadiness on turbine blade leading edge heat flux. *J. Eng. Gas Turbines Power.* **2012**, *134*, 071901. [CrossRef]
11. Wang, Y.A.; Li, L.B.; Zhang, J.Z. Study on the interaction between coolant pulsation and recir- culation vortexes by large-eddy simulation. *Aerosp. Sci. Technol.* **2022**, *130*, 107951. [CrossRef]
12. Babaee, H.; Acharya, S.; Wan, X. Optimization of forcing parameters of film cooling effecti- veness. *J. Turbomach.* **2014**, *136*, 061016. [CrossRef]
13. Adamovich, I.; Baalrud, S.; Bogaerts, A.; Bruggeman, P.; Cappelli, M.; Colombo, V.; Czarnetzki, U.; Ebert, U.; Eden, J.; Favia, P. The 2017 Plasma Roadmap: Low temperature plasma science and technology. *J. Phys. D Appl. Phys.* **2017**, *50*, 323001. [CrossRef]
14. Corke, T.C.; Post, M.L.; Orlov, D.M. Single dielectric barrier discharge plasma enhanced aerodynamics: Physics, modeling and applications. *Exp. Fluids* **2009**, *46*, 1–26. [CrossRef]
15. Benmoussa, A.; Rodrigues, F.F.; Páscoa, J.C. Plasma Actuators for Cycloidal Rotor Thrust Vectoring Enhancement in Airships. *Actuators* **2023**, *12*, 436. [CrossRef]
16. Benmoussa, A.; Pascoa , J.C. Performance improvement and start-up characteristics of a cyclorotor using multiple plasma actuators. *Meccanica* **2021**, *56*, 2707–2730.
17. Daraee, M.A.; Abbasi, S. A novel approach to performance improvement of a VAWT usingplasma actuators. *J. Clean. Prod.* **2023**, *424*, 138876. [CrossRef]
18. Yang, P.Y.; Zhang, X.; Pan, C. The spatial-temporal evolution process of flow field generated by a pulsed-DC plasma actuator in quiescent air. *Aerosp. Sci. Technol.* **2021**, *118*, 107071. [CrossRef]
19. Roya, S.; Wang, C.C. Plasma actuated heat transfer. *Appl. Phys. Lett.* **2008**, *92*, 231501. [CrossRef]
20. Singh, K.P.; Roy, S. Modeling Plasma Actuators with Air Chemistry for Effective Flow Control. *J. Appl. Phys.* **2007**, *101*, 1233308. [CrossRef]
21. Pescini, E.; Martínez, D.S.; De Giorgi, M.G.; Ficarella, A. Optimization of microsingle dielectric barrier discharge plasma actuator models based on experimental velocity and body force fields. *Acta Astronaut.* **2015**, *116*, 318–332. [CrossRef]
22. Roya, S.; Wang, C.C. Numerical Investigation of three-dimensional plasma actuation for improving film cooling effectiveness. *J. Thermophys. Heat Transf.* **2013**, *27*, 489–497. [CrossRef]
23. Yu, J.L.; He, L.M.; Zhu, Y.F.; Ding, W.; Wang, Y.Q. Numerical simulation of the effect of plasma aerodynamic actuation on improving film hole cooling performance. *Heat Mass Transf.* **2013**, *49*, 897–906. [CrossRef]
24. Dai, S.J.; Xiao, Y.; He, L.M.; Jin, T.; Zhang, Q.; Hou, P.H.; Zhao, Z.C. Film-cooling of cylindrical hole with downstream surface dielectric barrier discharge actuators. *Int. J. Heat Mass Transf.* **2015**, *90*, 825–837. [CrossRef]
25. Xiao, Y.; Dai, S.J.; He, L.M.; Jin, T.; Zhang, Q.; Hou, P.H. Investigation of film cooling from cylindrical hole with plasma actuator on flat plate. *Heat Mass Transf.* **2016**, *52*, 1571–1583. [CrossRef]
26. Dolati, S.; Amanifard, N.; Deylami, H.M. Numerical study and GMDH-type neural networks modeling of plasma actuator effects on the film cooling over a flat plate. *Appl. Therm. Eng.* **2017**, *123*, 734–745. [CrossRef]
27. Audier, P.; Fénot, M.; Bénard, N.; Moreau, E. Film cooling effectiveness enhancement using surface dielectric barrier discharge plasma actuator. *Int. J. Heat Fluid. Flow.* **2016**, *62*, 247–257. [CrossRef]
28. Li, G.Z.; Zhang, H.J.; Yan, W.W. Control of the coherent structure dynamics of a film cooling flow by plasma aerodynamic actuation. *Int. J. Heat Mass Transf.* **2019**, *137*, 434–445. [CrossRef]
29. Li, G.Z.; Wang, Q.Q.; Huang, Y.J.; Zhang, H.J. Large eddy simulation of film cooling effectiveness on a turbine vane pressure side with a saw-tooth plasma actuator. *Aerosp. Sci. Technol.* **2021**, *112*, 106615. [CrossRef]

30. Jukes, T.N.; Choi, K.S.; Johnson, G.A.; Scott, S.J. Turbulent Drag Reduction by Surface Plasma through Spanwise Flow Oscil-lation. In Proceedings of the 3rd AIAA Flow Control Conference, Barcelona, Spain, 8–11 May 2006; AIAA 2006-3693.
31. Dai, S.J.; Xiao, Y.; He, L.M.; Jin, T.; Zhang, Q.; Hou, P.H.; Zhao, Z.C. An Experimental Study of Plasma Aerodynamic Actuation on a Round Jet in Cross Flow. *AIP Adv.* **2015**, *5*, 037143-10. [CrossRef]
32. Sinha, A.K.; Bogard, D.G.; Crawford, M.E. Film-cooling effectiveness downstream of a single row of holes with variable density ratio. *J. Turbomach.* **1991**, *113*, 442–449. [CrossRef]
33. Kohli, A.; Bogard, D.G. Adiabatic effectiveness, thermal fields, and velocity fields for film cooling with large angle injection. *J. Turbomach.* **1997**, *119*, 352–358. [CrossRef]
34. Shur, M.L.; Spalart, P.R.; Strelets, M.K.; Travin, A.K. A hybrid RANS-LES approach with delayed-DES and wall-modelled LES capabilities. *Int. J. Heat Fluid. Flow.* **2008**, *29*, 1638–1649. [CrossRef]
35. Roth, J.R.; Sherman, D.M.; Wilkinson, S.P. Electrohydrodynamic flow control with a glow-discharge surface plasma. *AIAA J.* **2000**, *38*, 1166–1172. [CrossRef]
36. Corke, T.C.; Post, M.L. Overview of plasma flow control: Concepts, optimization, and applications. In Proceedings of the 43rd AIAA Aerospace Sciences Meeting and Exhibit, Reno, NV, USA, 10–13 January 2005. Paper No. 2005-0563. [CrossRef]
37. Shyy, W.; Jayaraman, B.; Andersson, A. Modeling of glow discharge-induced fluid dynamics. *J. Appl. Phys.* **2002**, *92*, 6434–6443. [CrossRef]
38. Zhang, P.F.; Liu, A.B.; Wang, J.Z. Flow structures in flat plate boundary layer induced by pulsed plasma actuator. *Sci. China Tech. Sci.* **2010**, *53*, 2772–2782. [CrossRef]
39. Rizzetta, D.P.; Visbal, M.R. Large eddy simulation of plasma-based turbulent boundary layer separation control. *AIAA J.* **2010**, *48*, 2793–2810. [CrossRef]
40. Hunt, J.C.R.; Wray, A.A.; Moin, P. Eddies, streams, and convergence zones in turbulent flows. In *Proceedings of the 1988 Summer Program*; Center for Turbulence Research, Stanford University: Stanford, CA, USA, 1988.
41. Wang, C.H.; Wang, J.Z.; Feng, H.K.; Huang, Y. Large eddy simulation of film cooling flowfrom a fanshaped hole. *Appl. Therm. Eng.* **2018**, *129*, 855–870. [CrossRef]